REVIEW

Theoretical Aspects on Doped-Zirconia for Solid Oxide Fuel Cells: from Structure to Conductivity

Shu-hui Guan[a,b], Zhi-pan Liu[b*]

a. Shanghai Academy of Agricultural Sciences, Shanghai 201403, China
b. Collaborative Innovation Center of Chemistry for Energy Material, Shanghai Key Laboratory of molecular Catalysis and Innovative Materials, Key Laboratory of Computational Physical Science, Department of Chemistry, Fudan University, Shanghai 200438, China

(Dated: Received on March 14, 2021; Accepted on April 7, 2021)

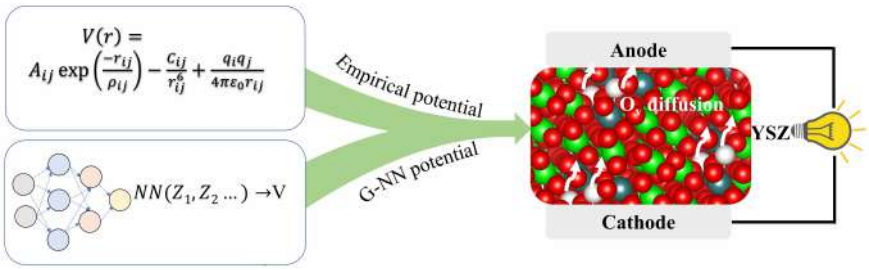

Solid oxide fuel cells (SOFCs) are regarded to be a key clean energy system to convert chemical energy (*e.g.* H_2 and O_2) into electrical energy with high efficiency, low carbon footprint, and fuel flexibility. The electrolyte, typically doped zirconia, is the "state of the heart" of the fuel cell technologies, determining the performance and the operating temperature of the overall cells. Yttria stabilized zirconia (YSZ) have been widely used in SOFC due to its excellent oxide ion conductivity at high temperature. The composition and temperature dependence of the conductivity has been hotly studied in experiment and, more recently, by theoretical simulations. The characterization of the atomic structure for the mixed oxide system with different compositions is the key for elucidating the conductivity behavior, which, however, is of great challenge to both experiment and theory. This review presents recent theoretical progress on the structure and conductivity of YSZ electrolyte. We compare different theoretical methods and their results, outlining the merits and deficiencies of the methods. We highlight the recent results achieved by using stochastic surface walking global optimization with global neural network potential (SSW-NN) method, which appear to agree with available experimental data. The advent of machine-learning atomic simulation provides an affordable, efficient and accurate way to understand the complex material phenomena as encountered in solid electrolyte. The future research directions for design better electrolytes are also discussed.

Key words: Solid oxide fuel cells, Yttria stabilized zirconia, Conductivity, Atomistic structure, Theoretical aspects

I. ELECTROLYTE MATERIALS OF SOFC

Solid oxide fuel cells (SOFCs) as an electrochemical energy conversion device have received considerable attention in the past decades for their many advantages (high energy conversion efficiency, low operation, and maintenance cost, negligible pollution, *etc.*) [1–3]. It consists of three primary components, *i.e.* cathode, anode, and electrolyte, where the solid dense electrolyte is sandwiched by two porous electrodes (FIG. 1(a)). The electrolyte determines largely the performance and the

*Author to whom correspondence should be addressed. E-mail: zpliu@fudan.edu.cn

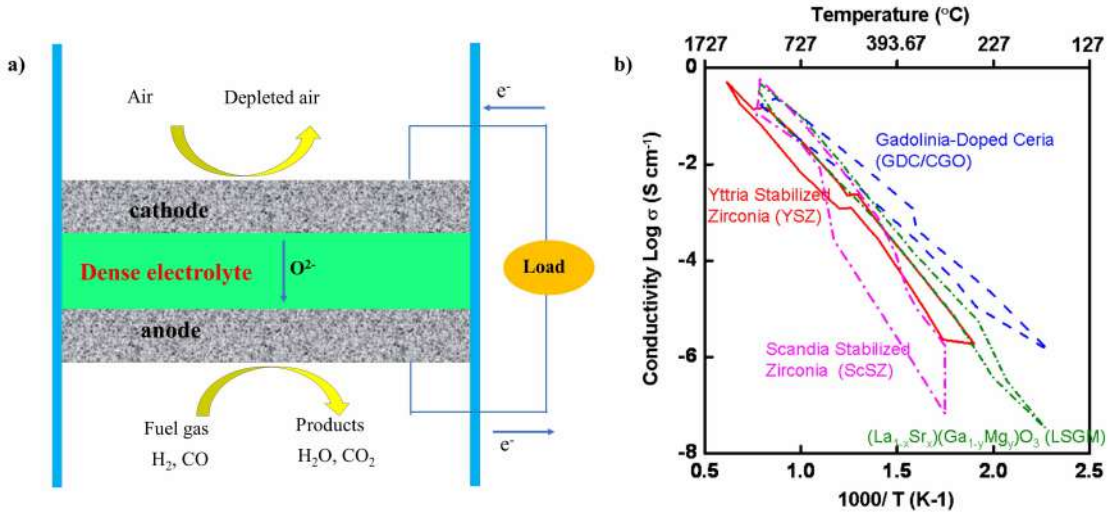

FIG. 1 (a) The illustration of operating principle of SOFC application. (b) The conductivity of several representative SOFC electrolyte materials [5].

operating temperature of the overall cells, and thus its material has been the major concern of research development. The basic requirements for an excellent electrolyte include the high ionic conductivity, the low electrically conductivity, the chemical and mechanical stability. A variety of oxide combinations have been considered for SOFC in history, which can be summarized as six categories [4] as detailed in the following. The conductivity of representative electrolytes [5] is illustrated in FIG. 1(b).

A. Doped ceria

CeO_2 with a fluorite structure, based electrolytes were recently used as an interlayer together with YSZ in bi-layer electrolyte to prevent interaction between cobaltite-based perovskite cathode and YSZ based electrolyte due to its good compatibility with electrodes, and also become the promising conductors for intermediate-temperature (600−800 °C) or low-temperature (<600 °C) SOFC due to its high ion conductivity at low temperature [6]. The dopants are typically trivalent (Gd^{3+}, Sm^{3+}, Y^{3+}) or divalent (Ca^{2+}) ions. Charge compensation occurs by the formation of oxygen vacancies and these defects are mobile species. The best ionic conductors were found to be Gd_2O_3-doped CeO_2 (GDC) and Sm_2O_3-doped CeO_2 (SDC) [7] with the conductivity of 0.030 and 0.041 S/cm at 700 °C, respectively. But doped ceria electrolyte materials are a mixture of ionic and electrically conducting (MIEC) oxide and therefore theoretically lead to a decrease in the voltage because of the partial reduction of Ce^{4+} to Ce^{3+} in the reducing atmosphere.

B. Stabilized bismuth oxide

Stabilized δ-Bi_2O_3 with a fluorite type structure has a high ionic conductivity compared to other solid electrolytes, which is due to the highly defective oxygen sublattice [7]. The dopants into bismuth can be rare-earth elements such as Y, Dy, Gd, or Er and their combinations with higher valence cations, such as V, W or Nb [8]. The maximum conductivity was reported to be 0.23 S/cm at 650 °C in 20 mol% Er-stabilized δ-Bi_2O_3 (ESB) [8]. The material cannot be used for intermediate temperature SOFC due to its low stability in the reducing atmosphere. It also possess other disadvantages, including volatilization of bismuth oxide at elevated temperatures, a high corrosion activity and low mechanical strength.

C. $LaGaO_3$ based electrolytes

Perovskite-type $LaGaO_3$ based electrolyte, in the general formula of $La_{1-x}Sr_xGa_{1-y}Mg_yO_{3-d}$ (LSGM), can have high ionic conductivity and stability in dual atmospheres, recognized as one of the promising electrolyte for intermediate temperature SOFCs [9]. The high conductivity in $LaGaO_3$ can be achieved by substituting La^{3+} with alkaline earth elements and/or incorporating divalent metal cations, such as Mg^{2+}, into gallium sublattice, which increases the concentration of oxygen vacancies (O_v). For example, (Sr, Mg)-

DOI:10.1063/1674-0068/cjcp2103044

doped $LaGaO_3$ with x=0.10−0.20, and y=0.15−0.20 ($La_{0.9}Sr_{0.1}Ga_{0.8}Mg_{0.2}O_{3-d}$) reaches the conductivity at 0.11−0.14 S/cm at 800 °C. To date, LSGM electrolyte is still less employed because of many practical issues, such as the phase instability, the mechanical stability, the volatility of gallium at high temperatures and the reaction with NiO (anode materials) in forming insulating $LaNiO_3$ phase [5].

D. Proton conducting electrolytes

Perovskite-type proton conducting oxides including $SrZrO_3$, $SrCeO_3$, $BaCeO_3$ and $BaZrO_3$-based solid solutions are also regarded as a promising type of solid electrolyte for intermediate temperature SOFC [7]. Proton conduction is believed to be based on the existence of proton defects in the oxide, which are created when oxide-containing oxygen vacancies dissociate and absorb water from the surrounding wet atmosphere. The ionic conductivity of the BaO_3 (ZrO_3, CeO_3, LnO_3) perovskite family can reach 0.01−0.1 S/cm at 600−700 °C [10]. The chemical instability of the materials also impedes the real applications as they are reactive with CO_2.

E. CeO_2-carbonate composite electrolytes

The composite based on CeO_2 and its eutectic mixture of Na_2CO_3, Li_2CO_3 and K_2CO_3 salts are well-known electrolytes for low-temperature SOFCs [11]. The SDC/$(Li\text{-}Na)_2CO_3$ is reported to have a maximum conductivity of 0.1 S/cm at low temperatures (300−600 °C). This excellent property of ceria/carbonate composite is attributed to the multi-ion conduction in the fuel cell atmosphere, where the interfaces between the constituent phases act as "superionic highways" for achieving the high ionic conduction [12]. The volatility of the molten carbonate is the key concern in applications.

F. Zirconia-based solid electrolyte

This is the most common and popular electrolyte, where the conductivity originates from the diffusion of oxygen ions (O^{2-}). The stabilizing dopants can be CaO, MgO, Y_2O_3, Sc_2O_3 and certain rare earth oxides such as Nd_2O_3, Sm_2O_3, Yb_2O_3 [13]. Among them, Y_2O_3 stabilized zirconia (YSZ) was mostly studied, in which a tiny amount of element yttrium added to the zirconia during manufacture can help to achieve a high ionic conductivity at high temperatures. Sc-stabilized zirconia (ScSZ) is another important stabilized zirconia electrolyte material, which has so far the highest ionic conductivity (0.30 S/cm at 1000 °C with 11 mol% Sc_2O_3) [14], presumably because of the similar ionic radii of the Sc^{3+} (0.87 Å) and the Zr^{4+} ions (0.84 Å). The major limitations of ScSZ are the availability and cost of Sc element together with the long-term stability [15]. In this review, we will focus on YSZ system that has received most theoretical attentions and is the testing ground for different theoretical methods.

II. YSZ ELECTROLYTE

Now we focus on the representative SOFC electrolyte material, YSZ. The history of YSZ electrolyte can be dated back to 1960s. It is known that the introduction of yttria enhances greatly the mechanical and chemical stability of zirconia under the typical operating conditions (high temperature ∼800−1000 °C), which fulfills the high performance requirement of the electrochemical system, including the high oxygen ionic conductivity properties, the high stability of chemical and mechanical resistance [2, 16–20]. However, the high operating temperature poses a problem to the SOFC durability by inducing the degradation of cell components and also increases the difficulty for the mobile applications. Therefore, recent decades have seen persistent efforts to enhance the performance towards lowering the operating temperature [20, 21]. Various modifications have been proven to be effective, such as reducing the film of electrolyte component, introducing the metal oxide inside the YSZ (*e.g.* Sc, Y-codoped [22, 23]) and fabricating bilayer electrolyte (*e.g.* YSZ/GDC, YSZ/SDC).

From a fundamental point of view, a number of key facts have been gleaned from experimental studies on the ionic conductivity of YSZ: (i) the ion conductivity peaks at a particular low Y/Zr ratio [24–28] at the operating temperatures, *i.e.* 8 mol% Y_2O_3 (8YSZ) with typically 0.1−0.2 S/cm at 1273 °C [29], but not at the compositions with higher Y concentration and stoichiometrically more O_v; (ii) The conductivity of 8YSZ drops remarkably [30–32] within less than 1000 h under 1000 °C working condition; (iii) while the conductivity increases with the lift of temperature, the high temperature and the low temperature regions exhibit distinct activation energies (E_a) according to the Arrhenius plot [33–37]. The E_a in 8YSZ is 0.70 eV at high temperatures (>1073 K) [29, 37], but increases to 0.96−1.16 eV

DOI:10.1063/1674-0068/cjcp2103044

at low temperatures (<973 K) [36, 38]. Due to the limitation of experimental techniques at the high temperatures, it remains largely unclear on how O anion diffuse in YSZ transport.

These observations have been the subjects of theoretical studies with the aim to understand the origin of the conductivity and to design better materials. A first step of theoretical studies is to determine the atom position of YSZ at different composition, which helps to answer the fundamental questions, such as where Y and O_v reside in ZrO_2. The more challenging task to theoretical simulation is to trace the atom motion and finally determine the O anion transport properties at different compositions and temperatures. Indeed, a large volume of theoretical studies have been performed on the YSZ system in the past 25 years using different simulation techniques, from the force field calculations to first principles calculations and more recently to the machine-learning potential calculations [39]. The purpose of the review is to overview the theoretical results from different models and identify the further challenges to theoretical methods in simulating the complex material system. We will show that the SSW-NN provides a powerful platform to resolve the atomic structure which can lead to the prediction of ionic conductivity and ion transport process.

III. THEORETICAL STUDIES OF YSZ FROM STRUCTURE TO CONDUCTIVITY

A. Theoretical methods

Theoretical simulations have been the major tool in the field to understand the conductivity phenomena at the atomic level. Most standard simulation methods have been utilized in this field, such as density functional theory (DFT) [40–42], kinetic Monte Carlo (KMC) [43], and molecular dynamics simulations (MD) [44–51]. DFT simulation could achieve high accuracy in describing the PES, but it is generally limited to hundreds of atoms and thus fails to describe the microstructure of low doping YSZ (*e.g.* 8YSZ) where the large cells in modeling are required. KMC is an effective tool to study the diffusion processes involving infrequent events, but it becomes frustrated when a system can undergo a large structural change due to the discrete on-lattice approximation applied in KMC simulation.

Not surprisingly, in the past years MD simulations based on empirical force field potentials, *e.g.* usually in the form of Born-Mayer-Huggins (BMH) potential [52, 53] was most-widely used to treat the YSZ systems. This force field potential has the general BMH form given by Eq.(1) [54]:

$$\varphi(r) = A_{ij} \exp\left(\frac{-r_{ij}}{\rho_{ij}}\right) - \frac{C_{ij}}{r_{ij}^6} + \frac{q_i q_j}{4\pi\varepsilon_0 r_{ij}} \qquad (1)$$

It includes three terms, the repulsive potential between ionic cores, the van der Vaals interaction and the Coulomb's interaction. In the equation, r_{ij} is the distance between a pair of ions i and j, q is the point charge of an ion, and the parameters A, ρ, and C can be determined by fitting to known experimental properties, or the energy surface determined by DFT calculations, or a combination thereof. While the potential form is kept, different sets of parameters have been proposed for YSZ in different reports, see Table I. As shown, the interaction between cations (*e.g.* Zr−Zr) is generally described by pure Coulomb potential without considering the dispersion and short-ranged repulsion terms (A_{ij}=0). The formal charges are used for all ions, *i.e.* −2 for oxygen, +4 for zirconium and +3 for yttrium. For the simplicity of the mathematic form, large-scale MD simulations with the BMH potentials can be conveniently performed using standard force-field packages, including LAMMPS, GULP and GROMACS. We will overview the key results from these simulations in Section III.C and III.D.

The potential parameters from Bulter *et al.* was used for simulating the defect structure of ZrO_2 [55], but this model will collapse when two oxygen ions are too close to each other due to an overly strong O−O interaction. Potential parameters from Cormack and Catlow are derived according to the properties of the tetrahedral ZrO_2 [56]. Brinkman model [52] derived by Dwivedi and Cormack suffers from the problem that the structure of ZrO_2 prefers to form the orthorhombic phase rather than the lower-symmetry monoclinic, which also exists in Schelling model [57]. The potential parameters from Lau and Dunlap are found to be unstable for YSZ systems above 1500 K [58].

As a promising alternative to force-field based methods, the stochastic surface walking global optimization with global neural network potential (SSW-NN) method [39, 59] developed recently demonstrates its superior advantages for solving the complex material problems [60, 61]. Compared to DFT calculations, NN

DOI:10.1063/1674-0068/cjcp2103044

TABLE I Parameters of the BMH potential used for the yttrium-stabilized zirconia in literatures.

Reference	Interaction	A/(kJ/mol)	ρ/nm	C/(kJ·mol^{-1}·nm^{-6})
Butler *et al.* [55]	$Zr^{4+}-O^{2-}$	9.7780×10^4	0.03764	1.3828×10^{-4}
	$Y^{3+}-O^{2-}$	7.5726×10^4	0.03587	0
	$O^{2-}-O^{2-}$	2.0861×10^6	0.0149	1.0264×10^{-2}
Cormack and Catlow [56]	$Zr^{4+}-O^{2-}$	1.3322×10^5	0.035	0
	$Y^{3+}-O^{2-}$	7.5726×10^4	0.03587	0
	$O^{2-}-O^{2-}$	2.0861×10^6	0.0149	2.55839×10^{-3}
Brinkman *et al.* [52]	$Zr^{4+}-O^{2-}$	9.5120×10^4	0.03760	0
	$Y^{3+}-O^{2-}$	1.2978×10^5	0.03490	0
	$O^{2-}-O^{2-}$	2.1960×10^6	0.01490	2.6910×10^{-3}
Schelling *et al.* [57]	$Zr^{4+}-O^{2-}$	1.4493×10^5	0.03450	
	$Y^{3+}-O^{2-}$	1.3183×10^5	0.03480	
	$O^{2-}-O^{2-}$	9.2123×10^5	0.2240	1.8911×10^{-3}
Lau and Dunlap [58]	$Zr^{4+}-O^{2-}$	1.2474×10^5	0.03584	1.8684×10^{-3}
	$Y^{3+}-O^{2-}$	1.5858×10^5	0.03532	1.0052×10^{-2}
	$O^{2-}-O^{2-}$	1.2638×10^6	0.02197	4.7567×10^{-3}

potential can be at least four orders of magnitude faster, and unlike force field potentials, NN potential is able to describe chemical reactions with high accuracy as long as the training dataset contains the reactive data. This provides the unique chance for NN potential to solve complex atomic movement problems that require both accuracy and long-time simulation. In particular, SSW-NN method is a convenient and efficient tool to establish the global PES for material and obtain the global minimum (GM). In the past several years our group has mapped out the PESs for a number of systems, *e.g.* single element crystal (boron) [62], molecular crystal (ice) [63], metal oxide (TiO_2) [64], ternary metal oxides ($ZnCr_2O_4$) [65].

The first machine learning potential for the Y-Zr-O ternary system, *i.e.*, the YZrO global neural network (G-NN) potential was established recently by using SSW-NN method. Specifically, more than 10^7 structures on $Y_{2x}Zr_{1-2x}O_{2-x}$ global PES were visited by SSW-NN during NN potential generation, which include metallic Zr and different oxide compositions (ZrO_x, Y_2O_3, and $Y_{2x}Zr_{1-2x}O_{2-x}$ with Y/Zr=∼1:9 to ∼4:3) in different morphologies (bulk, surfaces, and clusters). The final training dataset consists of 28803 structures that are selected to represent the global PES. The G-NN potential adopts the feed-forward NN architecture with five layers (188-60-50-50-1) for each element, reaching 71103 fitting parameters in total. The root-mean-square-error (RMSE) of the potential is 7.674 meV/atom and 0.165 eV/Å for energy and force, respectively [60, 61]. SSW-NN method is implemented in LASP program (www.lasphub.com), which includes a variety of common atomic simulation tools. As a key feature, LASP provides several TS search and SSW global optimization methods, which have been well tested in heterogeneous catalysis and solid phase transition [63, 65, 66].

B. PES exploration and atomic structures of YSZ

Because of the structural complexity of YSZ system, theoretical methods to characterize the atomic structure need to be fast and reliable to evaluate the energetics of structures and also be highly efficient to explore the large structural phase space. In fact, there are only a few attempts to resolve the atomic structures of YSZ. Based on DFT calculations, Predith *et al.* [67] obtained the convex hull of YSZ with the Y concentration from 12.3 mol% to 80.2 mol% in a small system size (<40 atom). Although they did not explicitly obtain the structure and energetics of 8YSZ, they suggested that 8YSZ was thermodynamically unstable. Later, Chen *et al.* [68]. searched for the ground state of 8YSZ by using empirical potential calculations, revealing that vacancy favored in the first nearest neighbor (1NN), 3NN and 5NN of Zr for the lowest energy structure. Parkes *et al.* [40] studied the atomistic structure of 6.7YSZ using DFT, and found that oxygen vacancies

DOI:10.1063/1674-0068/cjcp2103044

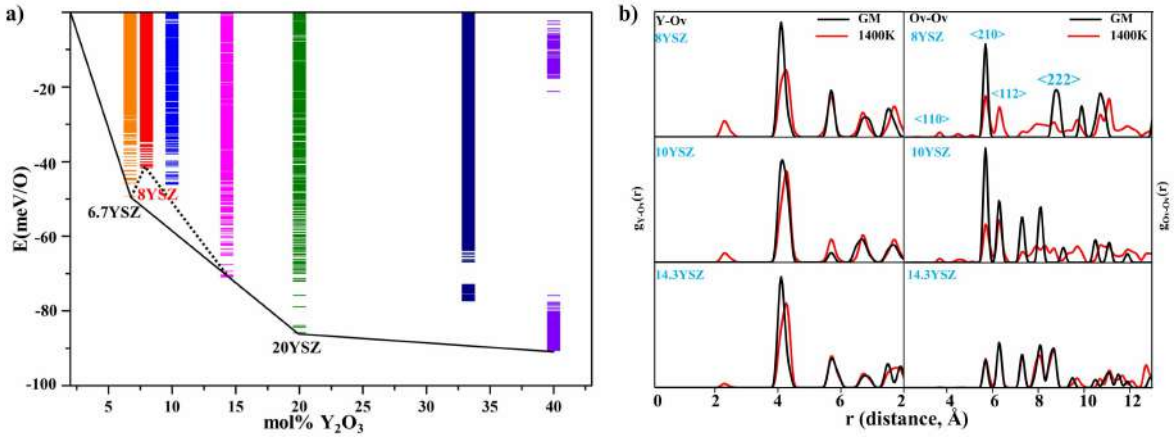

FIG. 2 (a) Thermodynamic convex hull diagram for $Y_{2x}Zr_{1-2x}O_{2-x}$ with respect to the cubic-ZrO_2 and cubic-Y_2O_3 (as the energy zero). The energy spectrum for low energy structures in each composition is shown as the color bars. Adapted with permission of Ref.[61] ©American Institute of Physics). (b) Radial distribution function $g(r)$ of the Y−O_v (left panel) and O_v−O_v (right panel) pairs at 1400 K from MD simulation and those of the GM for 8YSZ, 10YSZ, and 14.3 YSZ. Adapted with permission of Ref.[60] ©American Chemical Society.

orientated along the ⟨210⟩ direction.

With the advent of SSW-NN simulation, the global PES of YSZ can be systematically explored. Recently, we reported the GMs for seven concentrations of $Y_{2x}Zr_{1-2x}O_{2-x}$. Thermodynamic convex hull and GM structures of YSZ are established, as shown in FIG. 2(a). It is obvious that the diagram has three convex points at 6.7, 20, and 40 mol%, *i.e.* 6.7YSZ, 20YSZ and 40YSZ, corresponding to the thermodynamics stable phases. While the most concerned 8YSZ is not a convex point, indicating the phase is thermodynamically unstable, consistent with previous results based on DFT [67]. Both 33.3YSZ and 40YSZ are new ordered phases, namely, $Zr_2Y_2O_7$, a cubic pyrochlore structure (FD-3M, #227) for 33.3YSZ and $Zr_3Y_4O_{12}$, a rhombohedral structure (R-3, #148) for 40YSZ named as δ phase in experiments. We note that the experiment [69] has shown that as early as ∼20% Y concentration, the δ phase (40YSZ) starts to appear. This in fact also suggests that the structure with Y concentration between 20% and 40% are thermodynamically unstable, which agrees with the prediction from our convex hull. For the low Y concentration below 20%, both monoclinic and cubic phases are observed in experiments, again in agreement with the dual convex points at 6.7% (a monoclinic phase) and at 20% (distorted cubic phase) from theory.

The radial distribution functions (RDFs) can be utilized to understand the ordering of atoms in a real space. As shown in FIG. 2(b) (black line), the cation-vacancy RDFs of GM in 8YSZ from SSW-NN method show that O_v has a strong tendency to locate only nearby Zr cation as the 1NN. The O_v−O_v RDFs show that the peaks appear at ⟨210⟩ and ⟨222⟩ direction. In addition, Y cations tend to form Y-O-Y pairs, aligning along ⟨110⟩ with the nearest Y−Y distance being 3.7 Å in 8YSZ. With the increase of dopant concentration, O_v−O_v RDFs show that the peaks at ⟨112⟩ direction become strong, but they have very low (or zero) intensity at the ⟨222⟩ direction.

To characterize the atomic structures at finite temperatures, MD simulations have been utilized starting from large YSZ supercells in a cubic ZrO_2 structure. These initial structures are often obtained from the random configurations, where the Zr atoms are chosen at random to be replaced by yttrium and randomly selected oxygen atoms are also removed to ensure the charge balance [46, 51]. Alternatively, the global optimization can be also utilized to determine the most stable structure of YSZ at different composition, from which the initial structure is generated.

MD simulations based on force-field potential show that there is a preference for vacancies to locate at the nearest neighbors to Zr^{4+} cations at 1200 K [23, 46] (FIG. 3(a)). The O_v−O_v RDFs (FIG. 3(b)) show that there is a strong tendency for vacancies to form pairs in ⟨111⟩ directions, which suggests that the O_v−O_v pairs tend to be ordered at high temperatures. The similar trend of vacancy distribution was also found for 11YSZ at room temperature by MD simulations [51].

In contrast, MD simulations based on G-NN potential at 1400 K show that the two peaks in O_v−O_v RDFs at

DOI:10.1063/1674-0068/cjcp2103044

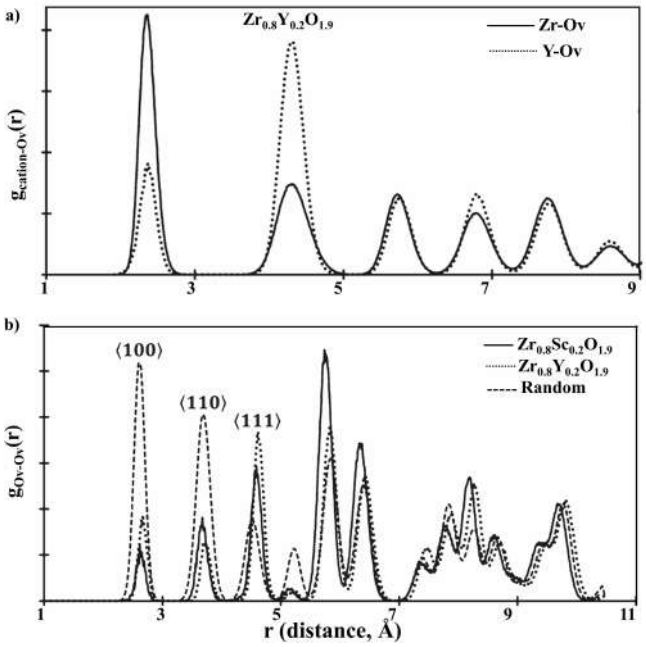

FIG. 3 Radial distribution function $g(r)$ of (a) the cation-O_v pairs and (b) O_v-O_v pairs at 1200 K from MD simulation based on empirical potential. Adapted with permission of Ref.[23] ©American Chemical Society.

the ⟨210⟩ (∼5.8 Å) and ⟨112⟩ (∼6.2 Å) are the primary features in all three YSZ systems (8YSZ, 10YSZ and 14.3YSZ). Importantly, G-NN predicts only ⟨222⟩ peak, but does not support the presence of ⟨111⟩ peak. As shown in FIG. 2(b) (red line), the ⟨210⟩ peak remains as the highest peak as it is in the GM for 8YSZ, but the ⟨112⟩ peak becomes the highest peak for 10YSZ and 14.3YSZ at 1400 K.

These structural features from theory are generally consistent with experiment. For example, the preference of O_v to be nearby Zr is supported by experiments that the decrease in the 1NN coordination number of Zr ions occurs from 8 to 5.6 for 8YSZ at 1273 K over 1000 h using X-ray absorption fine structure (EXAFS) [70]. The preference of O_v along either ⟨111⟩ from force-field models or ⟨222⟩ from G-NN potential is supported by the diffraction studies of anion-deficient fluorite oxides in 8YSZ. The tendency to aggregate along ⟨112⟩ for O_v identified from G-NN potential at higher dopant concentrations is also supported by Goff *et al.* [71].

C. Anion diffusion kinetics of YSZ

To provide insights into the conductivity behavior of YSZ, the anion diffusion barrier has been measured in experiments using the techniques such as oxygen tracer diffusion (OTD), AC impedance spectroscopy and secondary ion mass spectrometry. Theoretical simulations based on MD and KMC have been carried out to compare with the experimental data, as summarized in Table II.

TABLE II Summary of experimental and calculated data (T, E_a) for the activation energy of oxygen bulk diffusion.

Composition	Method[a]	T/K	E_a[b]	Ref.
6YSZ	MD	1125−2500	0.59	[44]
8YSZ	MD	973−2000	0.45	[52]
8YSZ	MD	300−1500	0.79	[72]
8YSZ	MD	1000−2000	0.5	[73]
8YSZ	MD	1125−2500	0.60	[44]
8YSZ	MD	300−1400	0.59	[74]
8YSZ	MD	1500−3000	0.71	[75]
8YSZ	MD	1000−2000	0.67	[48]
8YSZ	MD	1000−2000	0.48	[49]
8YSZ	SSW-NN	800−1000	0.87	[60]
8YSZ	SSW-NN	1100−1800	0.63	[60]
8YSZ	KMC	1000−2200	0.60	[76]
8YSZ	SIMS	673−973	0.96	[38]
8YSZ	IS	1073−1573	0.70	[29]
8.3YSZ	KMC	600−1500	0.70	[41]
9.5YSZ	IS	523−833	1.11	[77]
9.5YSZ	IS	833−1473	0.89	[77]
9.5YSZ	OTD	723−923	0.91	[78]
9.5YSZ	OTD	923−1373	0.82	[78]
9.5YSZ	IS	523−1023	1.10	[78]
10YSZ	MD	1000−2000	0.6	[73]
10YSZ	MD	1125−2500	0.73	[44]
10YSZ	MD	1000−2000	0.55	[49]
12YSZ	MD	1500−3000	0.80	[75]
14YSZ	MD	1000−2000	0.60	[49]
15YSZ	MD	1500−3000	0.88	[75]
8-24YSZ	OTD	650−1200	0.8−1.0	[79]
8-10YSZ	OTD	65−1200	0.95	[80]

[a] KMC: kinetic Monte Carlo, OTD: oxygen tracer diffusion, SIMS: secondary ion mass spectrometry, IS: AC impedance spectroscopy.
[b] E_a is activation energy in eV.

As listed in Table II, theoretical calculations from MD and KMC methods based on force field calculations show that the activation energy for oxygen diffusion in 8YSZ is in a range of 0.45−0.71 eV. With the increase of the dopant concentration, the activation energy increases almost linearly [41, 49, 75, 81]. The O_v diffusion that follows the path along the Zr−Zr

DOI:10.1063/1674-0068/cjcp2103044

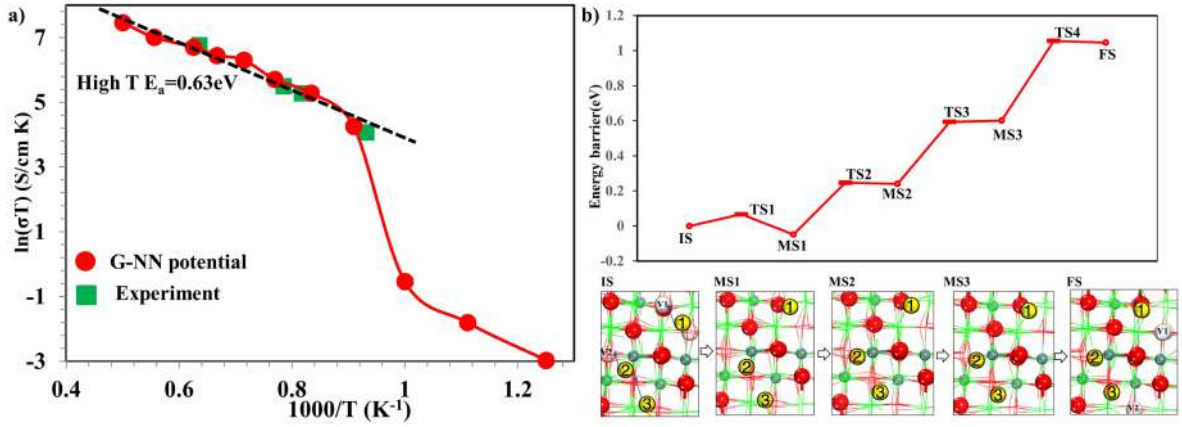

FIG. 4 (a) Arrhenius plot of the conductivity σ of 8YSZ with respect to temperature from 800 K to 2000 K. The activation energies are obtained from the slope of the linear fitting applied to low and high temperature ranges as indicated in the figure. Adapted with permission of Ref.[60] ©American Chemical Society. (b) The reaction pathway illustrating how O_v moves in 8YSZ at 1400 K. The Euclidean distance of the pathway is 4.74 Å. The reaction energy profile is shown in the top panel and the corresponding structure snapshots along the pathway are shown in the bottom. Y: dark green ball; reacting O: yellow balls with numbers (1, 2, 3), other resting O: red balls, vacancy: white balls labeled with V1 and V2. Adapted with permission of Ref.[60] ©American Chemical Society.

edge has a much lower barrier (∼0.6 eV) compared to those along the Y−Y (1.8 eV) or Y−Zr (1.2 eV) edges [76, 82]. However, the activation energy measured by different experiments are generally ∼1 eV [38, 79, 80]. For example, by using isotope ^{18}O tracer, Kilo *et al.* [79] measured the activation energy for O_v diffusion in YSZ with Y concentration ranging from 8 mol% to 24 mol% at 650−1200 K, and found that the activation energy is rather constant, ∼1 eV.

In general, the inconsistency between MD simulation and experiment may be caused by two factors: (i) the inaccuracy of the force field potentials, which has been known to yield a wrong energy ordering of low energy structures as benchmarked against density functional theory (DFT) calculations [40, 61]; (ii) the uncertainty on the exact YSZ structures in experiment, including the phase (monoclinic, cubic, tetragonal) and the Y (Zr) cation distribution. In previous force field simulations, the random initial structures from cubic ZrO_2 are generally adopted.

By starting from the GM structures from SSW-NN simulation, we have shown that the calculated lowest activation energy barrier at 0 K for 8YSZ and 10YSZ are the same, being 0.96 eV, involving the O_v diffusion along ⟨100⟩ between the neighboring 1NN positions. By inspecting the lowest energy pathways for O_v diffusion in 8YSZ, we found that there is the obvious diffusion over different cation-cation edges, *i.e.* Zr−Zr, Zr−Y (O_v is not nearby Y and thus no Y−Y edge diffusion channel is found).

At finite temperatures, the activation energies fitted from NN-based MD simulation for 8YSZ are 0.63 eV above 1100 K and 0.87 eV below 1000 K, as shown in FIG. 4(a). The anion diffusion pathways can be different from the pathway at 0 K. For example, a single O_v anion diffuses to its 3NN position along ⟨111⟩ direction; and more than one O_v anion move to its 1NN position along ⟨100⟩ direction. As shown in FIG. 4(b), we illustrate such a reaction, where two O_v anions move within 100 fs, one jumping to its 2NN position along ⟨110⟩ and the other to its 1NN position along ⟨100⟩.

The activation energies from NN simulation compare well with the experimental data, *i.e.* 0.70 and 0.96−1.16 eV for the high and low temperature regions respectively. The origin for the change of activation energy was thus revealed by analyzing the structure evolution of MD trajectory. It is apparent that at high temperatures, oxygen anions are no longer restrained to the lattice position, leading to intriguingly new features that are not present at low temperatures: (i) the formation of Y−O_v pairs; (ii) the increasing peak intensity at ⟨112⟩ direction; and (iii) the oscillation of the apparent O_v number, leading to an apparent lower O_v population than that in stichometry.

The activation energy from MD simulation for 10 YSZ is 0.84 eV above 1100 K, which is 0.14 eV higher than that of 8YSZ. This phenomenon is attributed to the stronger tendency of O_v aggregation at high tem-

DOI:10.1063/1674-0068/cjcp2103044

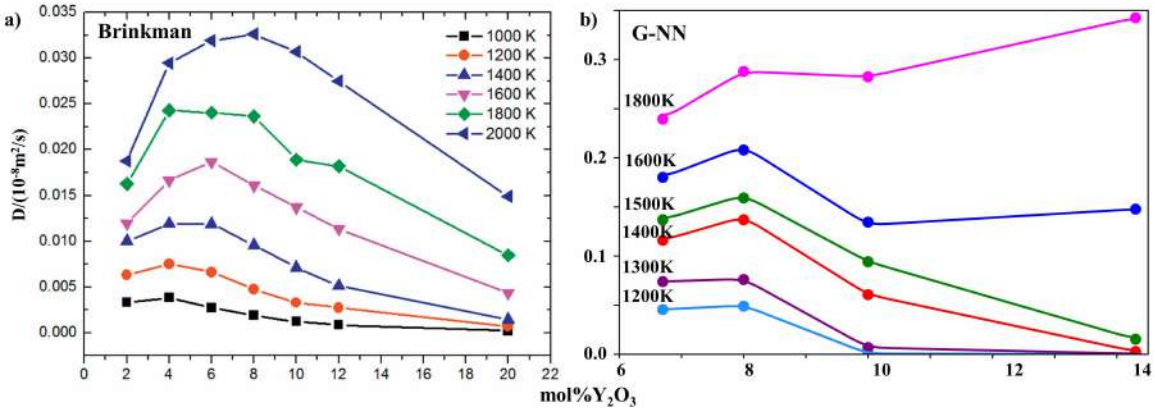

FIG. 5 (a) Oxygen diffusion coefficient D of oxygen *vs.* the concentration of Y_2O_3 at different temperatures using different models: (a) empirical potential from Brinkman model. Adapted with permission of Ref.[49] ©Wiley and (b) G-NN potential with permission of Ref.[60] ©American Chemical Society.

peratures in 10YSZ, which tends to align along ⟨112⟩ direction that hinders the O anion diffusion.

D. Ionic conductivity of YSZ

The ionic conducitivity is the key property for SOFC material. Ot can be measured using a DC (direct current) technique in experiment [83, 84]. In theory, the conductivity of oxygen ions σ is derived from the Nernst-Einstein relation in Eq.(2),

$$\sigma = \frac{q^2 DN}{V N_{\rm a}} \left(\frac{F^2}{RT} \right) \tag{2}$$

where $N_{\rm a}$ is the Avogadro constant, q is the charge of the mobile ion (2 for oxygen), N is the number of oxygen atoms, F is the Faraday's constant and D is the diffusion coefficient. The coefficient D can be obtained directly from MD simulation using Eq.(3), which corresponds to the slopes of mean square displacements of oxygen atom (Δr^2) plotted versus MD simulation time (t).

$$D = \lim_{t \to \infty} \frac{\langle \Delta r(t)^2 \rangle}{6t} \tag{3}$$

The relations between the calculated oxygen diffusion coefficients and YSZ concentrations have been reported from extensive literatures. All the results reproduced the two primary trends observed in experiment, *i.e.* the existence of a maximum and the dependence of the maximum position on temperature, as shown in FIG. 5(a). However, the positions of the peak from different force field not only deviate from the 8YSZ composition but also differ from each other. For example, the peak occurs at 5−7YSZ using Schelling and Brinkman models below 1600 K [48, 49], moving to 4YSZ below 1500 K using Brinkman models [45], and to 9.8YSZ using fitted parameters below 1300 K [51].

On the other hand, by starting from GM structures based on G-NN potential, we recently showed that the NN simulation can well reproduce the experimental observations. The NN simulation was carried out by performing a long-time MD simulation using LASP up to 2000 atoms with a wide temperature range from 800 K to 1800 K. As shown in FIG. 5(b), the peak occurs correctly at 8YSZ for a wide temperature range below 1600 K. With the increase of temperature to 2000 K, the maximum of D curve shifts from 8 mol% to the higher dopant concentrations. This trend was also noticed by Nakamura *et al.* [85] and Weller *et al.* [80] in experiment. The calculated conductivity for 14.3YSZ at 1600 K was 0.35 using NN potential [60], in good agreement with the experiment value of 0.30 at 1600 K. The calculated conductivity σ from G-NN potential of 8YSZ with 0.16−0.51 S/cm at 1200−1600 K compares well with 0.16−0.55 S/cm from experiment. This success to reproduce experimental data demonstrates the importance of the PES accuracy and the correct GM utilized as the initial configuration in MD simulation.

IV. CONCLUSION

This topic review presents recent theoretical progress on the structure and conductivity of Y-doped ZrO_2, a most utilized SOFC electrolyte material. Thanks to the rapid advance in theoretical methods, *i.e.* from force

DOI:10.1063/1674-0068/cjcp2103044

fields methods to first principles DFT, and to global neural network potential, the current understandings on the mechanism of the anion transport have reached the atomic level. The two key achievements are as follows.

(i) GM structures at different YSZ compositions are determined. The monoclinic phase is the GM for YSZ with Y concentration less than 8 mol%. 8YSZ is not a thermodynamics stable phase. (ii) Long-time structure evolution is obtained from MD simulation and the theoretical conductivity is derived. The O_v agglomeration along $\langle 112 \rangle$ that is typical for YSZ with Y concentration higher than 8 mol% is the major cause to retard the oxygen diffusion due to the strong $O_v - O_v$ repulsion.

These progress leads to understanding the intriguing phenomena observed in experiment, *e.g.* the maximum conductivity shifting to higher Y compositions above 1600 K and the non-Arrhenius behavior of conductivity around ∼1000 K. The other three-element solid ionic conductors, *e.g.* ScZrO, ScCeO, SmZrO, SmCeO [6, 13, 86, 87], should now be feasible to explore with the advent of the SSW-NN method.

Since it is the main goal to lower the operating temperature in SOFC applications, we expect that theoretical simulations should direct towards more complex systems, for example, with more dopants (*e.g.* Sc, Y-codoped), containing phase junctions (*e.g.* YSZ/GDC, YSZ/SDC), and involving grain boundaries [88]. The added complexity certainly poses new challenges to current theoretical methods. While SSW-NN holds a great promise in solving the challenging tasks of complex materials, one must bear in mind that a successful application of SSW-NN method relies much on the sampled dataset to the target problem. With the increase of structure and composition complexity, the building of NN potential becomes highly computational demanding. In particular, while the accuracy of NN potential can be improved, for example, by increasing the function complexity of structure descriptors to capture better physics, enlarging the number of fitting parameters in feed-forward NN and utilizing advanced network architectures, more challenging tasks would be developing new algorithms to reduce the computational cost for both quantum mechanics calculations and PES sampling in the coming years.

V. ACKNOWLEDGEMENTS

This work was supported by Shanghai Sailing Program (No.19YF1442800), the National Key Research and Development Program of China (No.2018YFA0208600), the National Natural Science Foundation of China (No.22003040, No.22033003, No.91945301, No.91745201, and No.21533001).

[1] A. B. Stambouli and E. Traversa, Sust. Energ. Rev. **6**, 433 (2002).
[2] B. C. Steele and A. Heinzel, Nature **414**, 345 (2001).
[3] N. Mahato, A. Banerjee, A. Gupta, S. Omar, and K. Balani, Prog. Mater. Sci **72**, 141 (2015).
[4] S. C. Singhal, *Solid Oxide Fuel Cells 15*, Pennington: Electrochemical Society Inc., 63 (2017).
[5] N. Laosiripojana, W. Wiyaratn, W. Kiatkittipong, A. Arpornwichanop, A. Soottitantawat, and S. Assabumrungrat, Eng. J. **13**, 65 (2009).
[6] N. Jaiswal, K. Tanwar, R. Suman, D. Kumar, S. Upadhyay, and O. Parkash, J. Alloys. Compd. **781**, 984 (2019).
[7] V. Kharton, F. Marques, and A. Atkinson, Solid State Ionics **174**, 135 (2004).
[8] P. Shuk, H. D. Wiemhofer, Ü. Guth, W. Gopel, and M. Greenblatt, Solid State Ionics **89**, 179 (1996).
[9] T. Ishihara, H. Matsuda, and Y. Takita, J. Am. Chem. Soc. **116**, 1994 (1994).
[10] F. Lefebvre-Joud, G. Gauthier, and J. Mougin, J. Appl. Electrochem. **39**, 535 (2009).
[11] B. Zhu, X. Liu, P. Zhou, X. Yang, Z. Zhu, and W. Zhu, Electrochem. Commun. **3**, 566 (2001).
[12] B. Zhu, S. Li, and B. E. Mellander, Electrochem. Commun. **10**, 302 (2008).
[13] T. Liu, X. F. Zhang, X. N. Wang, J. K. Yu, and L. Li, Ionics **22**, 2249 (2016).
[14] Y. Arachi, H. Sakai, O. Yamamoto, Y. Takeda, and N. Imanishai, Solid State Ionics **121**, 133 (1999).
[15] V. V. Lakshmi, R. Bauri, A. S. Gandhi, and S. Paul, Int. J. Hydrog. Energy **36**, 14936 (2011).
[16] E. Ryshkewitch, *Oxide Ceramics: Physical Chemistry and Technology*, New York: Academic Press, 350 (1960).
[17] S. Fabris, A. T. Paxton, and M. W. Finnis, Acta Mater **50**, 5171 (2002).
[18] A. Chroneos, B. Yildiz, A. Tarancón, D. Parfitt, and J. A. Kilner, Energ. Environ. Sci. **4**, 2774 (2011).
[19] M. Jaipal and A. Chatterjee, J. Phys. Chem. C **121**, 14534 (2017).
[20] Z. Zakaria, S. H. Abu Hassan, N. Shaari, A. Z. Yahaya, and Y. Boon Kar, Int. J. Energ. Res. **44**, 631 (2019).
[21] Z. Zakaria, Z. Awang Mat, S. H. Abu Hassan, and Y. Boon Kar, Int. J. Energ. Res. **44**, 594 (2019).
[22] F. Oksuzomer, S. Vatansever, S. N. Koc, H. Deligoz, M. A. Gurkaynak, and M. Somer, Int. J. Appl. Ceram.

DOI:10.1063/1674-0068/cjcp2103044

Technol. **8**, 42 (2011).
[23] S. T. Norberg, S. Hull, I. Ahmed, S. G. Eriksson, D. Marrocchelli, P. A. Madden, P. Li, and J. T. S. Irvine, System. Chem. Mater. **23**, 1356 (2011).
[24] R. E. W. Casselton, Phys. Status Solidi A **2**, 571 (1970).
[25] T. H. Etsell and S. N. Flengas, Chem. Rev. **70**, 339 (1970).
[26] M. Rühle, Adv. Mater. **9**, 195 (1997).
[27] O. Yamamoto, Y. Arachi, H. Sakai, Y. Takeda, N. Imanishi, Y. Mizutani, M. Kawai, and Y. Nakamura, Ionics **4**, 403 (1998).
[28] B. Butz, P. Kruse, H. Stormer, D. Gerthsen, A. Muller, A. Weber, and E. Iverstiffee, Solid State Ionics **177**, 3275 (2006).
[29] J. Kondoh, T. Kawashima, S. Kikuchi, Y. Tomii, and Y. Ito, J. Electrochem. Soc. **145**, 1527 (1998).
[30] F. T. Ciacchi and S. P. S. Badwal, J. Eur. Ceram. Soc. **7**, 197 (1991).
[31] M. Hattori, Y. Takeda, J. H. Lee, S. Ohara, K. Mukai, T. Fukui, S. Takahashi, Y. Sakaki, and A. Nakanishi, J. Power Sources **131**, 247 (2004).
[32] B. Butz, R. Schneider, D. Gerthsen, M. Schowalter, and A. Rosenauer, Acta Mater. **57**, 5480 (2009).
[33] X. Guo and J. Maier, J. Electrochem. Soc. **148**, E121 (2001).
[34] J. d. D. Solier, M. A. Perez-Jubindo, and H. Arturo, J. Am. Ceram. Soc. **72**, 1500 (1989).
[35] Y. Li, J. H. Gong, Y. S. Xie, and Y. F. Chen, J. Mater. Sci. Lett. **21**, 157 (2002).
[36] S. Komine and F. Munakata, J. Mater. Sci. **40**, 3887 (2005).
[37] A. Lakki, R. Herzog, M. Weller, H. Schubert, C. Reetz, O. Görke, M. Kilo, and G. Borchardt, J. Eur. Ceram. Soc. **20**, 285 (2000).
[38] R. A. De Souza, M. J. Pietrowski, U. Anselmi-Tamburini, S. Kim, Z. A. Munir, and M. Martin, Phys. Chem. Chem. Phys **10**, 2067 (2008).
[39] S. D. Huang, C. Shang, P. L. Kang, X. J. Zhang, and Z. P. Liu, Wiley Interdiscip. Rev.: Comput. Mol. Sci. **9**, e1415. (2019).
[40] M. A. Parkes, D. A. Tompsett, M. d'Avezac, G. J. Offer, N. P. Brandon, and N. M. Harrison, Phys. Chem. Chem. Phys. **18**, 31277 (2016).
[41] R. Pornprasertsuk, P. Ramanarayanan, C. B. Musgrave, and F. B. Prinz, J. Appl. Phys. **99**, 103513 (2005).
[42] A. Kushima and B. Yildiz, J. Mater. Chem. **20**, 4809 (2010).
[43] W. M. Kriven, A. L. Gyekenyesi, and J. Wang, *Developments in Strategic Materials and Computational Design*, Westerville: Amer Ceramic Soc., 193 (2011).
[44] R. Devanathan, W. Weber, S. Singhal, and J. Gale, Solid State Ionics **177**, 1251 (2006).
[45] W. Araki and Y. Arai, Solid State Ionics **181**, 1534 (2010).
[46] D. Marrocchelli, P. A. Madden, S. T. Norberg, and S. Hull, Chem. Mater. **23**, 1365 (2011).
[47] K. S. Chang, Y. F. Lin, and K. L. Tung, J. Power Sources **196**, 9322 (2011).
[48] V. V. Sizov, M. J. Lampinen, and A. Laaksonen, Solid State Ionics **266**, 29 (2014).
[49] H. C. Huang, P. C. Su, S. K. Kwak, R. Pornprasertsuk, and Y. J. Yoon, Fuel Cells **14**, 574 (2014).
[50] X. Li and B. Hafskjold, J. Phys.: Condens. Matter **7**, 1255 (1995).
[51] C. Yang, K. Trachenko, S. Hull, I. T. Todorov, and M. T. Dove, Phys. Rev. B **97**, 184107 (2018).
[52] H. W. Brinkman, W. J. Briels, and H. Verweij, Chem. Phys. Lett. **247**, 386 (1995).
[53] A. Dwivedi and A. N. Cormack, Philos. Mag. A **61**, 1 (1990).
[54] G. V. Lewis and C. R. A. Catlow, J. Phys. Solid State Phys. **18**, 1149 (1985).
[55] V. Butler, C. R. A. Catlow, and B. E. F. Fender, Solid State Ionics **5**, 539 (1981).
[56] A. N. Comack and C. R. A. Catlow, *Transport in Nomtoichiometric Compounds*, New York: Plenum Press, 101 (1985).
[57] P. K. Schelling, S. R. Phillpot, and D. Wolf, J. Am. Ceram. Soc. **84**, 1609 (2001).
[58] K. C. Lau and B. I. Dunlap, J. Phys.: Condens. Matter **23**, 035401 (2011).
[59] S. D. Huang, C. Shang, X. J. Zhang, and Z. P. Liu, Chem. Sci. **8**, 6327 (2017).
[60] S. H. Guan, C. Shang, and Z. P. Liu, J. Phys. Chem. C **124**, 15085 (2020).
[61] S. H. Guan, K. X. Zhang, C. Shang, and Z. P. Liu, J. Chem. Phys. **152**, 094703 (2020).
[62] S. D. Huang, C. Shang, P. L. Kang, and Z. P. Liu, Chem. Sci. **9**, 8644 (2018).
[63] S. H. Guan, C. Shang, S. D. Huang, and Z. P. Liu, J. Phys. Chem. C **122**, 29009 (2018).
[64] S. Ma, S. D. Huang, Y. H. Fang, and Z. P. Liu, ACS Appl. Energy Mater. **1**, 22 (2018).
[65] S. C. Ma, S. D. Huang, and Z. P. Liu, Nat. Catal. **2**, 671 (2019).
[66] S. C. Ma, C. Shang, and Z. P Liu, J. Chem. Phys. **151**, 050901 (2019).
[67] A. Predith, G. Ceder, C. Wolverton, K. Persson, and T. Mueller, Phys. Rev. B **77**, 144104 (2008).
[68] Y. Dong, L. Qi, J. Li, and I. W. Chen, Acta Mater. **127**, 73 (2017).
[69] Y. Suzuki, Solid State Ionics **81**, 211 (1995).
[70] J. Kondoh, S. Kikuchi, Y. Tomii, and Y. Ito, J. Electrochem. Soc **145**, 1550 (1998).
[71] J. P. Goff, W. Hayes, S. Hull, M. T. Hutchings, and K.

DOI:10.1063/1674-0068/cjcp2103044

N. Clausen, Phys. Rev. B **59**, 14202 (1999).
[72] N. Sawaguchi and H. Ogawa, Solid State Ionics **128**, 183 (2000).
[73] T. Arima, K. Fukuyo, K. Idemitsu, and Y. Inagaki, J. Mol. Liquid **113**, 67 (2004).
[74] W. Araki and Y. Arai, Solid State Ionics **181**, 441 (2010).
[75] R. L. González-Romero, J. J. Meléndez, D. Gómez-García, F. L. Cumbrera, and A. Domínguez-Rodríguez, Solid State Ionics **219**, 1 (2012).
[76] R. Krishnamurthy, Y. G. Yoon, D. J. Srolovitz, and R. Car, J. Am. Ceram. Soc. **87**, 1821 (2004).
[77] M. Filal, C. Petot, M. Mokchah, and C. Chateau, Solid State Ionics **80**, 27 (1995).
[78] P. S. Manning, J. D. Sirman, R. A. De Souza, and J. A. Kilner, Solid State Ionics **100**, 1 (1997).
[79] M. Kilo, C. Argirusis, G. Borchardt, and R. A. Jackson, Phys. Chem. Chem. Phys. **5**, 2219 (2003).
[80] M. Weller, Solid State Ionics **175**, 409 (2004).
[81] M. Asadikiya and Y. Zhong, J. Mat. Sci. **53**, 1699 (2017).
[82] F. Shimojo, T. Okabe, F. Tachibana, M. Kobayashi, and H. Okazaki, J. Phys. Soc. Jpn. **61**, 2848 (1992).
[83] A. Szendrei, T. D. Sparks, and A. V. Virkar, J. Electrochem. Soc. **164**, F1543 (2017).
[84] J. Kondoh, T. Kawashima, S. Kikuchi, Y. Tomii, and Y. Ito, J. Electrochem. Soc. **145**, 1536 (1998).
[85] A. Nakamura and J. J. Bruce Wagner, J. Electrochem. Soc **133**, 1542 (1986).
[86] S. M. Yang, S. Lee, J. Jian, W. Zhang, P. Lu, Q. Jia, H. Wang, T. W. Noh, S. V. Kalinin, and J. L. MacManus-Driscoll, Nat. Commun. **6**, 8588 (2015).
[87] D. Marrocchelli, L. Sun, and B. Yildiz, J. Am. Chem. Soc. **137**, 4735 (2015).
[88] B. Feng, T. Yokoi, A. Kumamoto, M. Yoshiya, Y. Ikuhara, and N. Shibata, Nat. Commun. **7**, 11079 (2016).

DOI:10.1063/1674-0068/cjcp2103044